Prepared in cooperation with the Afghanistan Geological Survey, Ministry of Mines under the auspices of the Task Force for Business and Stability Operations, Department of Defense

Lineament Analysis of Mineral Areas of Interest in Afghanistan

By Bernard E. Hubbard, Thomas J. Mack, and Allyson L. Thompson

Open-File Report 2012–1048
USGS Afghanistan Project Product No. 233

U.S. Department of the Interior
U.S. Geological Survey

U.S. Department of the Interior
KEN SALAZAR, Secretary

U.S. Geological Survey
Marcia K. McNutt, Director

U.S. Geological Survey, Reston, Virginia 2012

For product and ordering information:
World Wide Web: http://www.usgs.gov/pubprod
Telephone: 1–888–ASK–USGS

For more information on the USGS—the Federal source for science about the Earth,
its natural and living resources, natural hazards, and the environment:
World Wide Web: http://www.usgs.gov
Telephone: 1–888–ASK–USGS

Suggested citation:
Hubbard, B.E., Mack, T.J., and Thompson, A.L., 2012, Lineament analysis of mineral areas of interest in Afghanistan: U.S. Geological Survey Open-File Report 2012–1048, 28 p., available only at http://pubs.usgs.gov/of/2012/1048.

Cover: Photograph of an example of a prominent curvilinear “geomorphic” feature (that is, lineament) mapped using both ASTER and Landsat imagery, measured in the field by T. Mack on August 6, 2010, and resulting from localized microtographic relief within the Dusar-Shaida copper and tin area of interest, Afghanistan.

Contents

Figures

Tables

Lineament Analysis of Mineral Areas of Interest in Afghanistan

By Bernard E. Hubbard, Thomas J. Mack, and Allyson Thompson

Introduction

During a preliminary mineral resource assessment of Afghanistan (Peters and others, 2007), 24 mineralized areas of interest (AOIs) were highlighted as the focus for future economic development throughout various parts of the country. In addition to located mineral resources of value, development of a viable mining industry in Afghanistan will require the location of suitable groundwater resources for drinking, processing of mineral ores for use or for export, and for agriculture and food production in areas surrounding and supporting future mining enterprises. This report and accompanying GIS datasets describe the results of both automated and manual mapping of lineaments throughout the 24 mineral occurrence AOIs described in detail by Peters and others (2007; 2011) and summarized in table 1. For this study, we define lineaments as "mappable linear or curvilinear features of a surface whose parts align in a straight or slightly curving relationship that may be the expression of a fault or other linear zones of weakness" as derived from remote sensing sources such as optical imagery, radar imagery or digital elevation models (DEMs) (Sabins, 2007).

Table 1. Summary of names of mineral areas of interest (AOI), their highlighted commodities (after Peters and others, 2007, 2011), and alpha/numeric designation used in this report. In order to facilitate cross-comparison with their respective geohydrologic summaries discussed in Peters and others (2011), our AOI numerical order follows that of Peters and others (2011) where AOIs numbered 2 through 15 highlight metallic and precious metal prospects, while AOIs numbered 17 through 26 highlight industrial minerals. Note that numbers 1 and 16 are not used.

Numerical Order of Discussion	Mineral AOI Name (in alphabetical order from Peters and others, 2007; 2011)
2	Aynak copper, cobalt and chromium
3	Badakshan gold
4	Balkhab VMS copper
5	Daykundi tin and tungsten
6	Dusar-Shaida copper and tin
7	Haji-Gak iron
8	Katawas gold
9	Kharnak-Kanja mercury
10	Kundalan copper and gold porphyry
11	Nalbandon lead and zinc
12	North Takhar gold-placer
13	Panjsher Valley emerald, iron and silver
14	Tourmaline tin-vein
15	Zarkashan copper and gold
17	Baghlan clay and gypsum
18	Bakhud fluorite
19	Dudkash industrial minerals
20	Ghunday-Achin magnesite and talc
21	Khanneshin carbonatite
22	Kunduz celestite
23	North Herat barium and limestone
24	Nuristan pegmatite
25	South Helman travertine
26	Takhar evaporate

Water wells in bedrock aquifers are generally more productive where boreholes intersect fractures or fracture zones. Lineament identification and analysis have long been used as a reconnaissance tool to identify such favorable conditions for groundwater resources in carbonate bedrock environments (Lattman and Parizek, 1964; Siddiqui and Parizek, 1971). More recently, lineament analysis has been used to identify areas of greater well yields in other bedrock settings, such as crystalline bedrock (Mabee and other, 1994; Moore and others, 2002). Lineaments provide an indication of bedrock areas that warrant further investigation for optimal water well placement. They may also indicate areas of preferential flow and storage of groundwater, and, thus, areas with a greater density of lineaments may indicate greater secondary porosity. Lineaments may indicate structurally trending mineralized areas (for example, Mars and Rowan, 2007), or locations of near-surface water resources, especially when surface vegetation growth coincides with lineaments.

The purpose of this report and accompanying GIS data is to provide lineament maps that give one indication of areas that warrant further investigation for optimal bedrock water-well placement within 24 target areas for mineral resources (Peters and others, 2011). These data may also support the identification of faults related to modern seismic hazards (for example, Wheeler and others, 2005; Ruleman and others, 2007), as well as support studies attempting to understand the relationship between

tectonic and structural controls on hydrothermal fluid flow, subsequent mineralization, and water-quality issues near mined and unmined mineral deposits (for example, Eppinger and others, 2007).

Automated Lineament Mapping

Table 2 summarizes the 27 Landsat-7 ETM+ scenes used for automated lineament mapping across much of Afghanistan, which are also depicted as overlapping, yellow-shaded path and rows within location figure 1.

Table 2. Landsat ETM+ image data used in manual and automated lineament mapping for yellow-shaded paths/rows shown in figure 1 (after Davis, 2006). Numeric designation for each mineral area of interest (AOI) is explained in table 1.

Landsat Scene ID	Mineral AOIs Covered (#, all or in part)	Solar Elevation Angle (degrees)	Center Latitude	Center Longitude
ELP151R036_7T20010928	20, 24	47.96	34.6110 N	71.6543 E
ELP152R034_7T20010802	3, 12	60.52	37.4782 N	70.9474 E
ELP152R035_7T20010802	13, 24, 26	61.11	36.0439 N	70.5284 E
ELP152R036_7T20011005	2, 13, 20, 24	45.77	34.6130 N	70.1216 E
ELP152R037_7T20001018	20	42.94	33.1784 N	69.7880 E
ELP153R034_7T20010708	3, 12, 22, 26	64.07	37.4774 N	69.4083 E
ELP153R035_7T20010708	13, 17, 19, 22, 26	64.49	36.0482 N	68.9902 E
ELP153R036_7T20000822	2, 7, 17	58.19	34.6113 N	68.5849 E
ELP153R037_7T20001025	8, 15	40.76	33.1808 N	68.2271 E
ELP154R035_7T20010629	4, 17, 19, 22	65.26	36.0489 N	67.4779 E
ELP154R036_7T20010629	4, 5, 7, 17	65.59	34.6182 N	67.0698 E
ELP154R037_7T20000525	5, 10, 15, 18	66.41	33.1810 N	66.6676 E
ELP154R038_7T20010629	10, 18	66.00	31.7496 N	66.2818 E
ELP155R036_7T20010503	5, 9, 11	62.01	34.6160 N	63.9870 E
ELP155R037_7T20010503	5, 9, 11, 18	62.63	33.1878 N	65.0803 E
ELP155R038_7T20010503	18	63.24	31.7511 N	64.6912 E
ELP155R039_7T20010503	21, 25	63.70	30.3176 N	64.3117 E
ELP155R040_7T20010503	25	64.14	28.8790 N	63.9390 E
ELP156R036_7T20010627	11, 23	65.72	34.6160 N	63.9870 E
ELP156R037_7T20010627	9	65.96	33.1843 N	63.5895 E
ELP156R038_7T20010510	none	64.52	31.7493 N	63.1516 E
ELP156R039_7T20010510	21, 25	64.94	30.3158 N	62.7724 E
ELP157R036_7T20010517	6, 23	64.62	34.6180 N	62.4094 E
ELP157R037_7T20010517	6, 14	65.11	33.1864 N	62.0113 E
ELP158R035_7T20010711	23	64.18	36.0457 N	61.2592 E
ELP158R036_7T20000708	6, 23	65.23	34.6103 N	60.8681 E
ELP158R037_7T20010625	6	66.09	33.1829 N	60.4928 E

Additional metadata and description of these 27 Landsat ETM+ scenes (including specific scene acquisition times in UTC) are provided by Davis (2006) and tabulated using scene path and row ID numerical order. All of the 27 scenes used here were acquired either during late spring (May), summer (June through August), or early fall (September) with high sun angles greater than 55–60°. Although high sun-angle scenes are preferable for spectral classification methods used to derive mineral and lithologic maps (for example, Mars and Rowan, 2007), low sun-angle scenes (for example, latest fall, winter, and earliest spring) that accentuate large-scale topographic differences in illumination are preferable for lineament mapping (Sabins, 2007). In this study, no attempt was made to correct erroneous lineaments, such as ridgelines and catchment boundaries that are usually enhanced under high sun-angle lighting conditions (for example, Hung and others, 2005). However, linearly shaped scene-edge boundaries were the most obvious erroneous lineaments and, thus, were eliminated where possible.

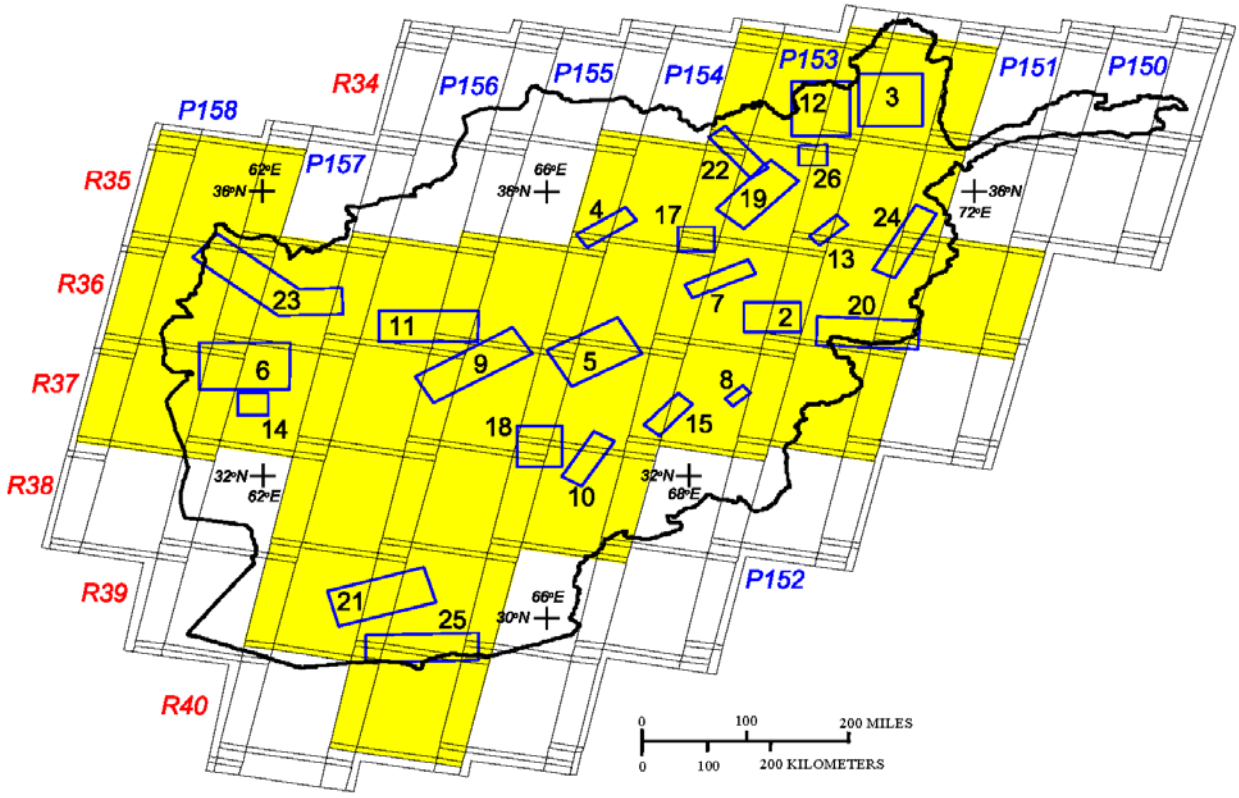

Figure 1. Landsat ETM+ scene orbital path (blue labeled) and row (red labeled) coverage map of Afghanistan, showing the locations of 24 numbered mineral occurrence areas of interest (Peters and others, 2007, 2011). Yellow-shaded scenes are listed in table 2. Also shown for clarity are overlapping scene boundaries and portions of scenes outside of the boundaries of Afghanistan.

The "Lineament Extraction" (LINE) algorithm of PCI Geomatica software was used to automatically extract lineaments from both the 30-m resolution Landsat-7 ETM+ multispectral band images and 15-m resolution Landsat-7 ETM+ panchromatic band images. Although several methods of pre-processing and image enhancements have been applied to multispectral data, such as Landsat and ASTER for enhancing geomorphic and tonal contrast related to lineaments (for example, principal components analysis, histogram-based stretch tools, band averages and, numerous filters; Walsh and

Mynar, 1986), the most effective method was found to be simple band average of all radiance values stretched to an 8-bit gray-scale range (Walsh and Mynar, 1986). Notably, band ratios were not used here because they tend to highlight spectral contrast at the expense of geomorphic and topographic contrast (Sabins, 2007). For the individual panchromatic band images of Landsat-7 ETM+, the original radiance values were used instead, though expanded to their full 8-bit monochrome dynamic display range.

The following input parameters were used and are documented in both the software user's manual (PCI, 2009) and recent supporting application references such as Hung and others (2005) and Abdullah and others (2009), who both successfully used the same PCI Geomatica software:

RADI = 24
GTHR = 94
LTHR = 50
FTHR = 7
ATHR = 40
DTHR = 30

RADI specifies the pixel distance of edge detection filtering such that smaller values can be used to detect more detail (that is, linear edges), but larger values can be used to minimize the detection of noise. RADI values can range from 0 to 8,192 pixels, but the default value is 10 pixels, whereas a value of 12 pixels was used by Abdullah and others (2009) and a value of 5 pixels was used by Hung and others (2005). GTHR specifies the minimum threshold change in brightness, which defines an edge pixel. GTHR values can range from 0 to 255 on an 8-bit pixel gray-scale. The default value is 100, though 90 was used by Abdullah and others (2009) and 10 was used by Hung and others (2005). LTHR specifies the minimum threshold of curvature (in pixel distance) used for mapping curved features as valid lineaments. Values of LTHR can range from 0 to 8,192 pixels, but the default value used by Abdullah and others (2009) is 30 pixels, and values of 7 and 3 pixels were used by Hung and others (2005) for ASTER and Landsat imagery, respectively. FTHR specifies the maximum error (in pixel distance) allowed in fitting a vector GIS arc or polyline to pixels defining a curved feature, such that lower values yield better fits using a number of shorter line and arc segments, while higher values yield coarser fits using longer lines and arcs with fewer segments. Values of FTHR can range from 0 to 8,192 pixels, but the default value used by Hung and others (2005) is 3 pixels, whereas a value of 10 pixels was used by Abdullah and others (2009). ATHR specifies the maximum angle (in degrees) between two neighboring polyline or arc segments, below which they can be linked into a single vector polyline or arc. Values of ATHR can range from 0 to 90°, with a default value of 30° as was used by Abdullah and others (2009), whereas a lower value of 7° was used by Hung and others (2005). DTHR specifies the minimum distance (in pixels) between the end points of two polyline or arcs for them to be linked, with possible values ranging from 0 to 8,192. The default value of DTHR is 20 pixels as was used by Abdullah and others (2009), whereas a lower value of 3 pixels was used by Hung and others (2005). The values for all of these parameters are used in a three-step execution process consisting of: edge detection, thresholding, and feature extraction (LINE module – PCI, 2009).

For this study, this set of parameter values best replicated the patterns of linearly trending vegetation, phyllic-mineralized areas, and mapped faults using the ASTER imagery within the Argandab igneous intrusive complex of Afghanistan, as rendered by Mars and Rowan (2007). These parameter values were also tested on ASTER scenes covering portions of the “Dushar-Shaida copper and tin” AOI (AOI 6, table 1 and figure 1) and "tourmaline tin-vein"-bearing AOI (AOI 14, table 1 and figure 1), both south of the city of Herat, Afghanistan. The resulting maps of lineament and vegetation features were then field checked by both aerial reconnaissance and field reconnaissance by Thomas Mack on August 6, 2010.

Hung and others (2005) tested the PCI algorithm using both Landsat ETM and ASTER imagery and found that ASTER 15-m resolution visible and near-infrared (VNIR) bands produced less noisy and more accurate lineament patterns than the equivalent Landsat 30-m resolution bands. Despite their lower 30-m resolution, the ASTER SWIR bands are still useful for mapping linearly trending spectral-tonal contrast related to epithermal phyllic alteration (for example, Mars and Rowan, 2007). In evaluating the spectral-tonal and geomorphic contrast characteristics of each of the six reflective bands of Landsat, Abdullah and others (2009) found that Landsat TM band 4 (as well as SPOT band 3) yields the highest number of lineaments, which is not surprising since it overlaps with the spectral range of the near infrared (NIR) reflective peak of vegetation. In contrast, Smith and Wise (2007) demonstrated enhanced numbers and increasing accuracy of lineaments mapped by using the higher spatial resolution panchromatic band (15 m for ETM+), instead of pre-processed gray-scale versions of the lower spatial resolution multispectral bands (30 m for ETM+). Therefore, using this understanding, we create automated lineament maps using both the multispectral and panchromatic Landsat ETM+ datasets.

Results from both image sets were compared to our preliminary field-checked ASTER mapping results that we obtained for the Dusar-Shaida area. The results derived from the 15-m panchromatic Landsat data appear to best match (based on visual inspection) the pattern and density of lineaments mapped using ASTER 15-m VNIR and 30-m SWIR band images (level 2 atmospherically corrected "at surface" radiance product, AST09), both of which were pre-processed to single monochrome images. The most obvious caveat with this parameterization approach is that lineament mapping results are being compared between two different multispectral image data types with differing spectral and spatial resolution characteristics, both acquired at two completely different times of year (May 17, 2001, for the ASTER imagery covering Dusar-Shaida and July 20, 2001, for the Landsat ETM+ imagery covering part of the same area). The consistency in the results between Landsat and ASTER for both this study and previously cited studies lends support for this approach.

Because of ASTER's limited swath-width (60 km) compared to that of Landsat (185 km) and variable off-nadir pointing, which produces inconsistent overlap between successive orbital swaths, the use of ASTER data for country-scale mapping of Afghanistan was impractical. Thus, we used both the 30-m resolution multispectral band and 15-m resolution panchromatic band images of Landsat-7 ETM+ to derive our country-scale lineament map coverages. Usage of low sun-angle Landsat scenes from the EROS Data Center archives was also considered impractical due to time constraints, as well as snow-cover and cloud-cover considerations that are more prevalent in low sun (winter) images.

The final seamless country-wide coverage was produced by first removing redundant lineaments from image overlap areas (fig. 1). For example, lineaments mapped in northern and eastern overlapping scenes were eliminated in favor of lineaments mapped in southern and western overlapping scenes. The merge tool of ARCGIS software was then used to reassemble all lineaments from both overlapping and nonoverlapping portions of Landsat swaths (fig. 1) back into country-scale coverages based on the two image datasets.

Secondly, lineaments mapped over flat basin and valley-fill areas represented by slope angles less than 2° (for example, Jayko and others, 2005), using slope data derived from ~90-m resolution Shuttle Radar Topography Mission (SRTM) digital elevation model (DEM), were also removed as explained further below. Figure 2 compares the distribution of areas characterized by less-than-2° slope angles with mapped Quaternary basin-fill deposits, lakes, and playas. Correlation between the two maps was calculated as 91.0586 percent (kappa coefficient = 0.7162) without including lakes and other sizable bodies of water, and 91.2260 percent (kappa coefficient = 0.7226) with lakes and other sizable bodies of water included as shown in figure 2*B*. The less-than-2° slope areas were then gap filled using a median filter with a seven SRTM pixel kernel, and used to exclude lineaments derived from the 30-m

multispectral and 15-m panchromatic band images of Landsat. The two resulting vector GIS shapefile coverages reflect lineaments mapped in higher slope (greater than 2°) bedrock areas, with most flat-basin and valley-fill areas containing anthropogenic features, such as roads and agricultural landuse patterns, for example, removed. These “higher sloping bedrock areas” should also include alluvial fans and pediments (for example, Jayko and others, 2005), which can also exhibit surface expressions of deeper-seated faulting (for example, Hooper and others, 2003; Ruleman and others, 2007), perhaps even related to buried aquifers. Finally, all other lineaments either outside the boundary of Afghanistan or outside the coverage of our SRTM data (from Peters and others, 2007) were eliminated.

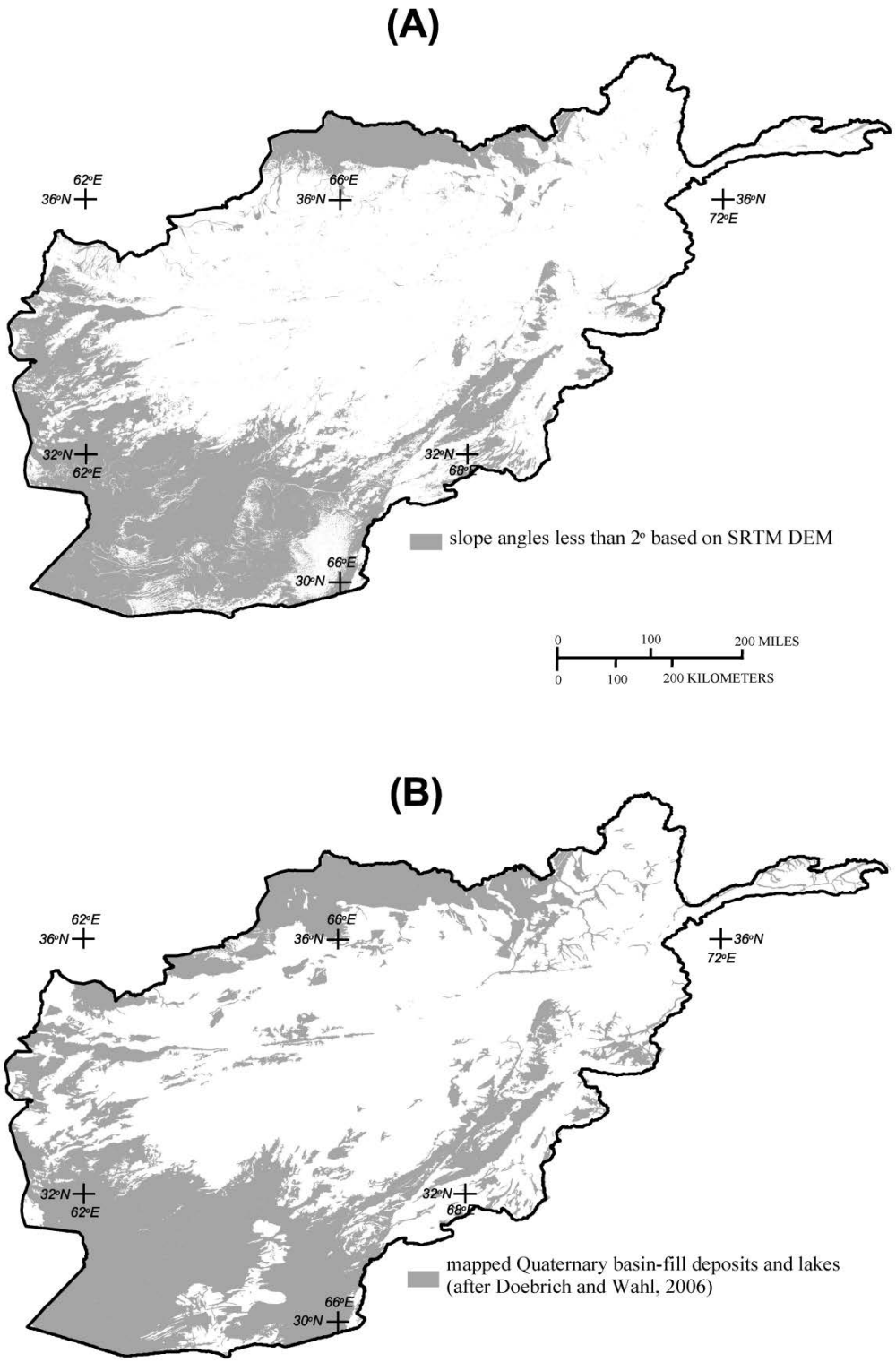

Figure 2. Areas characterized by slopes less than 2° as measured using the 90-m resolution SRTM DEM (*A*), compared with Quaternary basin-fill deposits, lakes, and playas mapped in Doebrich and Wahl (2006) (*B*).

Linear features mapped by automated (or visual) interpretation of optical remote-sensing data, such as Landsat TM imagery, can be caused by either highlights and shadows due to localized topographic relief (that is, geomorphic) or surface spectral discontinuities such as those caused by vegetation growth or soil moisture differences (that is, tonal). Additional spectral discontinuity may result from epithermal mineralization, and is best detected using sensors (for example, ASTER) with enhanced spectral resolution capability that can detect ferric-iron and phyllic [and (or) propylitic] alteration, in addition to other spectral discontinuities (for example, Mars and Rowan, 2007). Some linear features may represent cultural features, such as roads or canals, and may not represent a fracture zone. As such, automated-derived lineaments may require cross-comparison with other data sources, such as the manually derived lineaments as described in the following section, as well as follow-up field investigations to confirm the validity of the lineaments and their relation to water-filled bedrock fracture zones.

Manual Lineament Mapping

Lineaments were mapped using one observer, drawn at a map scale of 1:100,000, and using two datasets: (1) 30-m Shuttle Radar Topography Mission (SRTM) DEM data (Philip Davis, USGS, written commun., 2009) and (2) 14.25-m natural-color orthorectified Landsat mosaics (table 3) cut into 1:250,000 quadrangles by Davis (2006), and derived from the scenes listed in table 2 and shown in figure 1. Shaded-relief images were generated from the 30-m DEM using a 45° solar illumination angle at azimuth angles of 180°, 225°, 270°, and 315°. Linear features were initially identified on each of the four resulting SRTM shaded-relief images and then further refined using natural-color mosaic images. Features identified at one azimuth angle or using one sensor may not be apparent in another angle or using another sensor. Similarly, features identified using natural-color mosaics, particularly linear vegetation patterns, may not be apparent using the DEM data. Figure 3 shows the resulting distribution of lineaments derived manually and rendered for each AOI in Afghanistan, which are included in the accompanying vector GIS shapefile layer. Manually derived lineaments are stored in separate accompanying GIS shapefiles from those two sets derived automatically from Landsat multispectral band and panchromatic band images.

Table 3. Summary of Natural-Color Landsat Mosaic Images of Afghanistan, orthorectified and pan-sharpended to 15.25-m resolution by Davis (2006) and cut into the following 1:250,000-scale map quadrangles. Individual Landsat scenes covering all 24 mineral areas of interest and used in the following quadrangle map series are reported in table 2 after Davis (2006).

Landsat Natural-Color Image Mosaic Quadrangle Name
Q2962_14m_UTM_NC
Q2964_14m_UTM_NC
Q3062_14m_UTM_NC
Q3064_14m_UTM_NC
Q3162_14m_UTM_NC
Q3164_14m_UTM_NC
Q3262_14m_UTM_NC
Q3264_14m_UTM_NC
Q3266_14m_UTM_NC
Q3268_14m_UTM_NC
Q3360_14m_UTM_NC
Q3362_14m_UTM_NC
Q3364_14m_UTM_NC
Q3366_14m_UTM_NC
Q3368_14m_UTM_NC
Q3460_14m_UTM_NC
Q3462_14m_UTM_NC
Q3464_14m_UTM_NC
Q3466_14m_UTM_NC
Q3468_14m_UTM_NC
Q3470_14m_UTM_NC
Q3560_14m_UTM_NC
Q3564_14m_UTM_NC
Q3564_14m_UTM_NC
Q3568_14m_UTM_NC
Q3570_14m_UTM_NC
Q3664_14m_UTM_NC
Q3666_14m_UTM_NC
Q3668_14m_UTM_NC
Q3670_14m_UTM_NC
Q3764_14m_UTM_NC
Q3770_14m_UTM_NC

We applied our lineament identification criteria in a uniform manner during digitization within the 24 AOIs in an effort to improve identification objectivity. Field reconnaissance trips by Thomas Mack (USGS) in 2009 and 2010 provided additional familiarity with lineaments in various terranes and in several of the mineral areas of interest throughout Afghanistan. However, visual lineament identification is inherently subjective, particularly with respect to one observer, and in some locations it is possible that cultural features, such as irrigation canals and roads, topographic ridges, or other nonfracture-related features, may be mistaken for lineaments. As such, mapped lineaments require comparison with other data and field investigation to confirm their nature and relation to water-filled bedrock fracture zones.

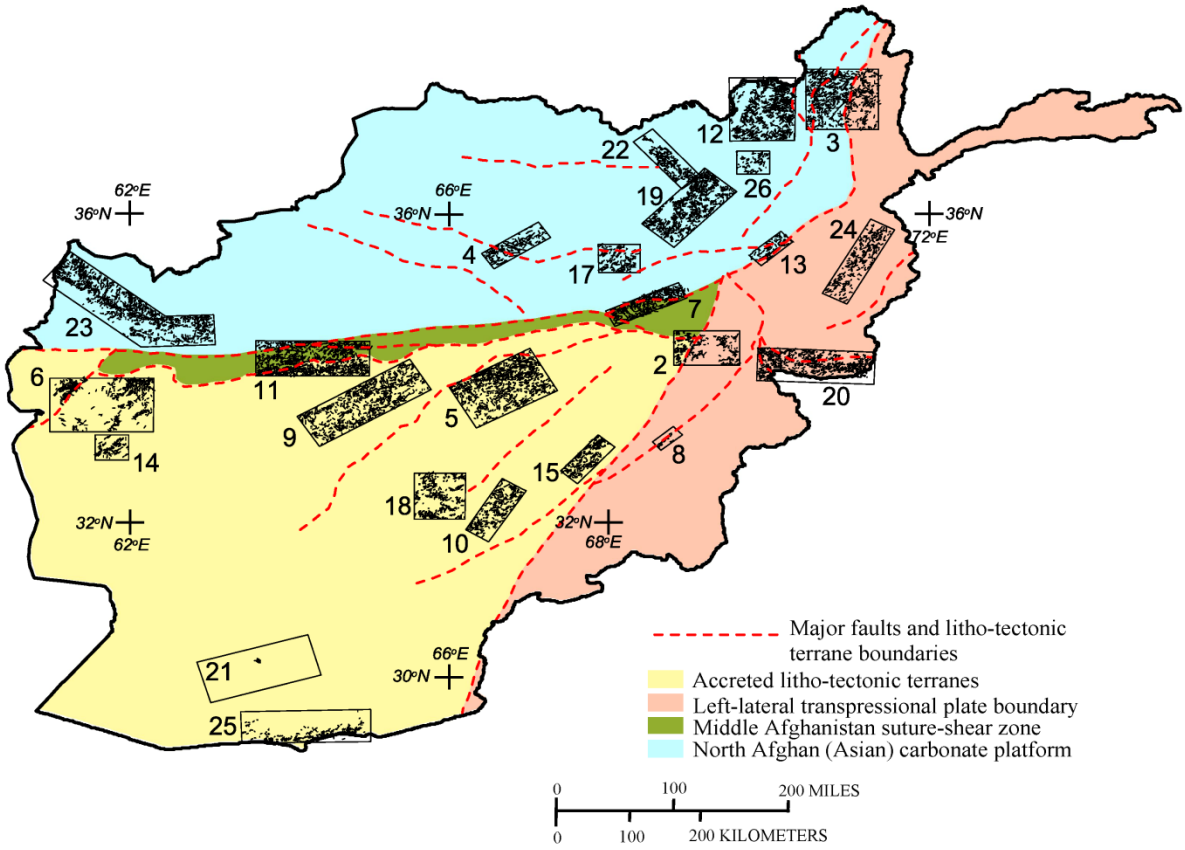

Figure 3. Manually mapped lineaments within the 24 mineral occurrence areas of interest (see also fig. 1 and table 2), superposed on the major tectonic regions and faults of Afghanistan for comparison. Modified after Wheeler and others (2005) and Ruleman and others (2007), the latter of which provides abbreviated fault names for dashed, red-colored fault boundaries shown above.

Results and Discussion

Accompanying this report are two sets of GIS lineament shapefiles automatically mapped using both the 30-m resolution multispectral Landsat ETM+ bands and the 15-m resolution panchromatic Landsat ETM+ bands, as well as a shapefile of lineaments derived manually using shaded-relief DEMs and pan-sharpened Landsat ETM+ quadrangle mosaics. Appendix 1 shows rose diagrams comparing the azimuth direction statistics for lineament populations derived manually and those derived automatically within the 24 mineral occurrence AOIs (figs. 1 and 3; table 2). Also shown are rose diagrams showing azimuth statistics of other previously mapped faults, fractures, folds and other structures mapped over Afghanistan (for example, Chmyriov and Mirzad, 1971; Abdullah and Chmyriov, 1977; Wheeler and others, 2005; Doebrich and Wahl, 2006) for which digital GIS versions were compiled by Peters and others (2007).

Most of the rose diagrams show an agreement in orientation azimuth. Azimuthal direction averages 45° NE–225° SW for lineaments derived automatically from the 30-m Landsat multispectral data, 41° NE–221° SW for lineaments derived automatically from the 15-m Landsat panchromatic data,

and 51° NE–230° SW for the manually derived lineament sets. These directions are within 25° of the dominant structural trends of the country, which parallel many of the faults bounding accreted lithotectonic terranes shown in figure 3. This level of agreement can be anticipated given the NE–SW orientations of most of the mineral occurrence AOIs (fig. 3), whose individual deposit locations are strongly controlled by prevailing regional tectonic trends (for example, Peters and others, 2007).

Because Landsat images are acquired over Afghanistan between 9:53 a.m. and 10:53 a.m. local time (for example, Davis, 2006), their solar azimuths are typically from the SE direction, regardless of the solar elevation angle variation with season. Therefore, subtle topographic variations associated with faults and fractures trending in the NW–SE directions are not accentuated by sunlight, which makes them difficult to detect visually by a human operator and even more difficult to detect by automated mapping algorithms (Sabins, 2007). An example of this is illustrated by the Balkhab (AOI4, fig. 3; appendix 1.4), Ghunday-Achin (AOI20, fig. 3; appendix 1.20), Khanneshin (AOI21, fig. 3; appendix 1.21), Kunduz (AOI22, fig. 3; appendix 1.22), and North Herat (AOI23, fig. 3; appendix 1.23) AOIs, which all contain large populations of mapped NW–SE-trending geologic structures. In all of these cases, except for Ghunday-Achin (AOI20), which was imaged with steep (less than 48°, table 2) sun-angle Landsat data, automated lineament mapping using both Landsat ETM+ dataset resolutions failed to capture many populations of NW–SE lineaments depicted in geologic maps. In the case of the Khanneshin and Kunduz AOIs, visual identification of lineaments successfully captured the NW – SE lineaments, perhaps due to the addition of DEM data represented by various solar azimuth light angles. Manual lineament plotting was somewhat successful in capturing NW – SE- trending lineaments in the North Herat AOI, but just as unsuccessful as automated methods in mapping such lineament trends within the Balkhab and Ghunday-Achin AOIs.

Based on similarities in mean azimuth and (or) the shape of the distribution of azimuth directions, the best agreement between the manual and automated lineament mapping occurs within the Kharnak-Kanja (AOI9, fig. 3; appendix 1.9), Nuristan (AOI24, fig. 3; appendix 1.24), and Zarkashan (AOI15, fig. 3; appendix 1.15) mineral occurrence AOIs. The latter AOI (Zarkashan, AOI 15, fig. 3) was partly mapped using Landsat imagery acquired at the lowest sun angle of 40.76° (table 2). Other notable areas of interest that yielded good agreement between linear structures depicted in geologic maps and those detected by either or both automated or manual image analysis are Aynak (AOI2, fig. 3; appendix 1.2), Katawas (AOI8, fig. 3; appendix 1.8), Nuristan (AOI24, fig. 3; appendix 1.24), and Panjsher Valley (AOI13, fig. 3; appendix 1.13). These four mineral occurrence AOIs were also imaged with the lowest sun angle (less than 48°, table 2) Landsat ETM+ data available.

Based on similarities in mean azimuth and (or) the shape distribution or number of lineaments with closely matching azimuths directions, good agreement between geologic map lineaments and manually derived lineaments also occurs within the Daykundi (AOI5, fig. 3; appendix 1.5), Dudkash (AOI19 – fig. 3; appendix 1.19), Takhar-evaporite (AOI26, fig. 3; appendix 1.26), and Tourmaline-tin (AOI14, fig. 3; appendix 1.14) mineral AOIs. Alternately, good agreement between mapped geologic lineaments and either or both of the automated mapped lineament sets occurs within the Bakhud (AOI18, fig. 3; appendix 1.18); Dusar-Shaida (AOI6, fig. 3; appendix 1.6); Haji-Gak (AOI7, fig. 3; appendix 1.7); Kundalan (AOI10, fig. 3; appendix 1.10); and Nalbandon (AOI11, fig. 3; appendix 1.11) mineral AOIs. Notably, the Dusar-Shaida AOI was field assessed for this study, with an example of a north–south (N–S)-trending lineament shown on the cover page.

In the North Takhar gold-placer AOI (AOI12, fig. 3; appendix 1.12), both sets of automated lineaments agree with each other and contain the most dominant azimuth trend (45° NE–SW) that is depicted by the manual mapping technique. However, both manual and automated sets of lineaments did not detect the predominant 11°–191° N–S orientations that are depicted in geologic maps. As expected,

the least reliable lineament datasets are those within the South Helman travertine AOI (AOI25, fig. 3; appendix 1.25) near the Pakistan border. The two automated (that agree with each other) and one manually derived lineament datasets disagree with the 75°–255° E–W directional trend of linear structures depicted on geologic maps of the area. This is not surprising since only high sun-angle Landsat ETM+ imagery (greater than 63.7°, table 2) was available, and the area is dominated by eolian deposits of the Helmand desert, as well as high clouds and dust streaks (or sand storms) within the imagery.

Both sets of automated mapped lineaments and the manually mapped lineaments provide complementary datasets for future GIS fracture density analysis and groundwater exploration (for example, Kim and others, 2004). For example, human visual interpretation is often the most effective way of identifying fault and fracture patterns at various solar illumination angles and image acquisition conditions. However, accurate fracture density analysis requires a statistically significant number of nonduplicated but representative sets of lineaments that most likely reflect the actual fracture patterns of subsurface rocks (Kim and others, 2004). As such, human operators do not always make reliable positive identification of lineaments, and different workers will often interpret linear features differently. In contrast to automated algorithms, manual digitizing of lineaments is time-consuming and rarely can produce the number of statistically representative lineaments needed for thorough and accurate fracture density analysis.

Problems with mapping lineaments oriented in a variety of directions both manually and automated can be reduced using imagery acquired during the seasons of lowest possible sun angle (if available and with minimal cloud- and snow-cover), and acquired with both morning and afternoon satellite passes that provide solar azimuths from the SE in the morning and the SW in the afternoon. However, because the most useful and highest spatial resolution optical sensors are in sun synchronous orbit, it is difficult to acquire morning imagery except in northern polar areas. Ancillary use of high quality (that is, noise-free) DEMs, shaded from various artificial light angles, may also assist in both manual and automated lineament mapping. Radar data sources, such as ALOS PALSAR, may provide additional opportunities to map lineaments using active remote sensing imagery acquired at different look or incident angles, and under all weather and lighting conditions. Finally, the lineament datasets generated in this study are being used to collectively assess overlapping areas of highest fracture density and potential as groundwater-aquifer resources across all 24 mineral AOIs in Afghanistan (for example, Peters and others, 2011). Two of these datasets (automated lineament mapping results) provide the statistical basis needed for typical fracture density analysis but contain more erroneous results due to limitations in current computer mapping algorithms. The other dataset (manual lineament mapping results) provides higher accuracy lineament maps due to superior abilities of the human visual cortex over computer algorithms but does not provide sufficient statistical basis for fracture density analysis due to the time-consuming and labor-intensive efforts required in digitizing them.

References Cited

Abdullah, Anwar, Akhir, J.M., and Abdullah, Ibrahim, 2009, A comparison of Landsat TM and SPOT data for lineament mapping in Hulu Lepar area, Pahang, Malaysia: European Journal of Scientific Research, v. 34, no. 3, p. 406–415.

Abdullah, S.H., and Chmyriov, V.M., 1977, Map of mineral resources of Afghanistan: Ministry of Mines and Industries of the Democratic Republic of Afghanistan, Department of Geological and Mineral Survey, scale 1:500,000.

Chmyriov, V.M., and Mirzad, S.H., eds., 1971, Tectonic map of Afghanistan: Kabul, Afghanistan, Ministry of Mines and Industries of Royal Afghanistan, Department of Geology and Mines, 4 sheets, scale 1:1,000,000.

Davis, P.A., 2006, Calibrated Landsat ETM+ Nonthermal-band image mosaics of Afghanistan: U.S. Geological Survey Open-File Report, OFR 2006–1345, 16 p., accessed September 15, 2011, at http://pubs.usgs.gov/of/2006/1345/.)

Doebrich, J.L., and Wahl, R.R., 2006, Geologic and mineral resource map of Afghanistan: U.S. Geological Survey Open-File Report 2006–1038, 1 pl. (Also available at http://pubs.usgs.gov/of/2006/1038/.)

Eppinger, R.G., Briggs, P.H., Dusel-Bacon, Cynthia, Giles, S.A., Gough, L.A., Hammarstrom, J.M., and Hubbard, B.E., 2007, Environmental geochemistry at Red Mountain, an unmined volcanogenic massive sulphide deposit in the Bonnifield district, Alaska Range, east-central Alaska: Geochemistry—Exploration, Environment, Analysis, v. 7, p. 207–233.

Hooper, D.M., Bursik, M.I., and Webb, F.H., 2003, Application of high-resolution, interferometric DEMs to geomorphic studies of fault scarps, Fish Lake Valley, Nevada-California, USA: Remote Sensing of Environment, v. 84, p. 255–267.

Hung, L.Q., Batelaan, Okke, and De Smedt, Florimond, 2005, Lineament extraction and analysis, comparison of Landsat ETM and ASTER imagery: Case study—Suoimuoi tropical karst catchment, Vietnam. in Remote Sensing for Environmental Monitoring, Volume V: GIS Applications and Geology, edited by Manfred Ehlers and Ulrich Michel,Proceedings of SPIE, v. 5983, 12 p.

Jayko, A.S., Menges, C.M., and Thompson, R.A., 2005, Digital method for regional mapping of surficial basin deposits in arid regions, Example from Central Death Valley, Inyo County, California: U. S. Geological Survey Open-File Report 2005–1445, 43 p., accessed September 15, 2011, at http://pubs.usgs.gov/of/2005/1445/.

Kim, G.B., Lee, J.Y., and Lee, K.K., 2004, Construction of lineament maps related to groundwater occurrence with ArcView and Avenue scripts: Computers and Geosciences, v. 30, p. 1117–1126.

Lattman, L.H., and Parizek, R.R., 1964, Relationship between fracture traces and the occurrence of ground water in carbonate rocks: Journal of Hydrology, v. 2, p. 73–91.

Mabee, S.B., Hardcastle, K.C., and Wise, D.U., 1994, A method of collecting and analyzing lineaments for regional-scale fractured-bedrock aquifer studies: Groundwater, v. 32, no. 6, p. 884–894.

Mars, J.C., and Rowan, L.C., 2007, Mapping phyllic and argillic-altered rocks in southeastern Afghanistan using Advanced Spaceborne Thermal Emission and Reflection Radiometer (ASTER) data: U.S. Geological Survey Open-file Report 2007–1006, single-page online poster format, accessed September 15, 2011, at http://pubs.usgs.gov/of/2007/1006/.

Moore, R.B., Schwarz, G.E., Clark, S.F., Jr., Walsh, G.J., and Degnan, J.R., 2002, Factors related to well yield in the fractured-bedrock aquifer of New Hampshire: U.S. Geological Survey Professional Paper 1660, 2 pls., 51 p., accessed September 15, 2011, at http://pubs.usgs.gov/pp/pp1660/.

PCI, 2009, Geomatica Version 10.3 Users Manual: PCI Geomatics Enterprises, Inc., Ontario, Canada, accessed September 29, 2011, at http://www.pcigeomatics.com/.

Peters, S.G., Ludington, S.D., Orris, G.J., Sutphin, D.M., Bliss, J.D., and Rytuba, J.J., 2007, Preliminary Non-Fuel Mineral Assessment of Afghanistan: U.S. Geological Survey Open-File Report 2007–1214, p. 810, accessed September 15, 2011, at http://pubs.usgs.gov/of/2007/1214/.

Peters, S.G., and others, 2011, Summaries of Important Areas for Mineral Investment and Production Opportunities in Afghanistan – Non-Fuel Minerals: U. S. Geological Survey Open-File Report 2011–1204, 1810 p. appendixes on DVD. (Also available at http://pubs.usgs.gov/of/2011/1204/.)

Ruleman, C.A., Crone, A.J., Machette, M.N., Haller, K.M., and Rukstales, K.S., 2007, Map and database of probable and possible Quaternary faults in Afghanistan: U.S. Geological Survey Open-File Report 2007–1103, 39 p., 1 pl, accessed September 15, 2011, at http://pubs.usgs.gov/of/2007/1103/.

Sabins, F.F., 2007, Remote Sensing: Principles and Interpretation (3d ed.): Long Grove, IL, Waveland Press, 512 p.

Siddiqui, S.H., and Parizek, R.R., 1971, Hydrogeologic factors influencing well yields in folded and faulted carbonate rocks in central Pennsylvania: Water Resources Research, v. 7, no. 5, p. 1295–1312.

Smith, M.J., and Wise, S.M., 2007, Problems of bias in mapping linear landforms from satellite imagery: International Journal of Applied Earth Observation and Geoinformation, v. 9, p. 65–78.

Walsh, S.J., and Mynar, Frank, III, 1986, Landsat digital enhancements for lineament detection: Environmental Geology and Water Science, Springer-Verlag, v. 8, no. 3, p. 123–128.

Wheeler, R.L., Bufe, C.G., Johnson, M.L., and Dart, R.L., 2005, Seismotectonic map of Afghanistan, with annotated bibliography: U.S. Geological Survey Open-File Report 2005–1264, 31 p., accessed September 29, 2011, at http://pubs.usgs.gov/of/2005/1264/].

Appendix 1

The following 12 pages are rose diagrams summarizing dominant azimuth directions for lineaments mapped within the mineral areas of interest (AOIs), numbered from 2 through 15 for metallic and precious metal prospects and 17 through 26 for industrial minerals, following the chapters describing geohydrologic summaries for each of the AOIs within Peters and others (2011). Note that numbers 1 and 16 are not used because they do not correspond to geohydrologic summary chapters within Peters and others (2011):

Aynak copper, cobalt and chromium area of interest (AOI, 1.2)

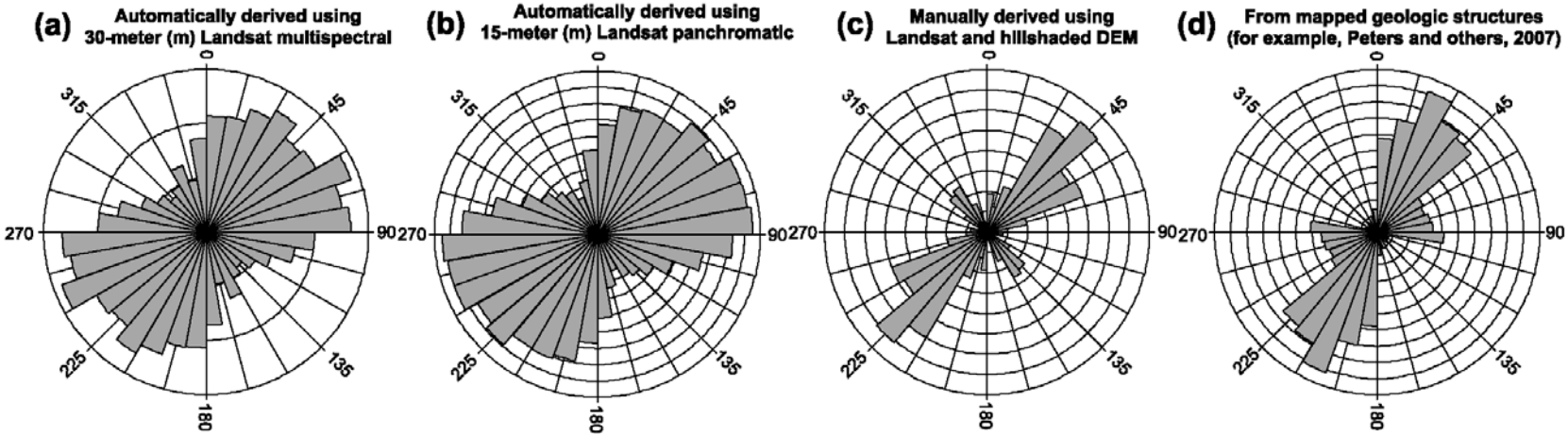

Badakhshan gold area of interest (AOI, 1.3)

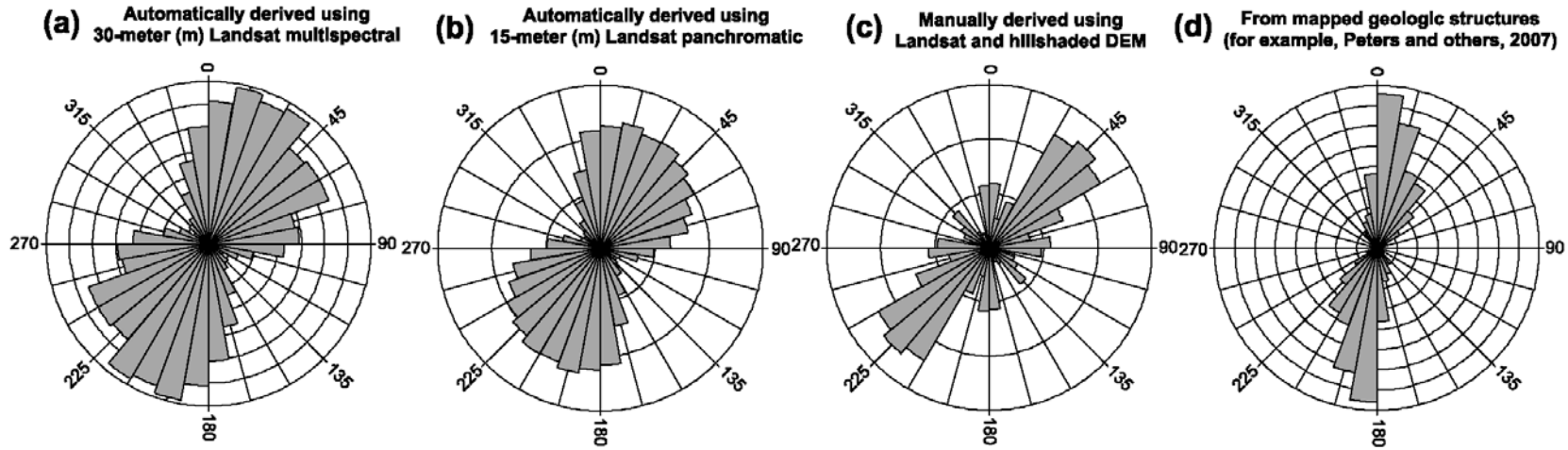

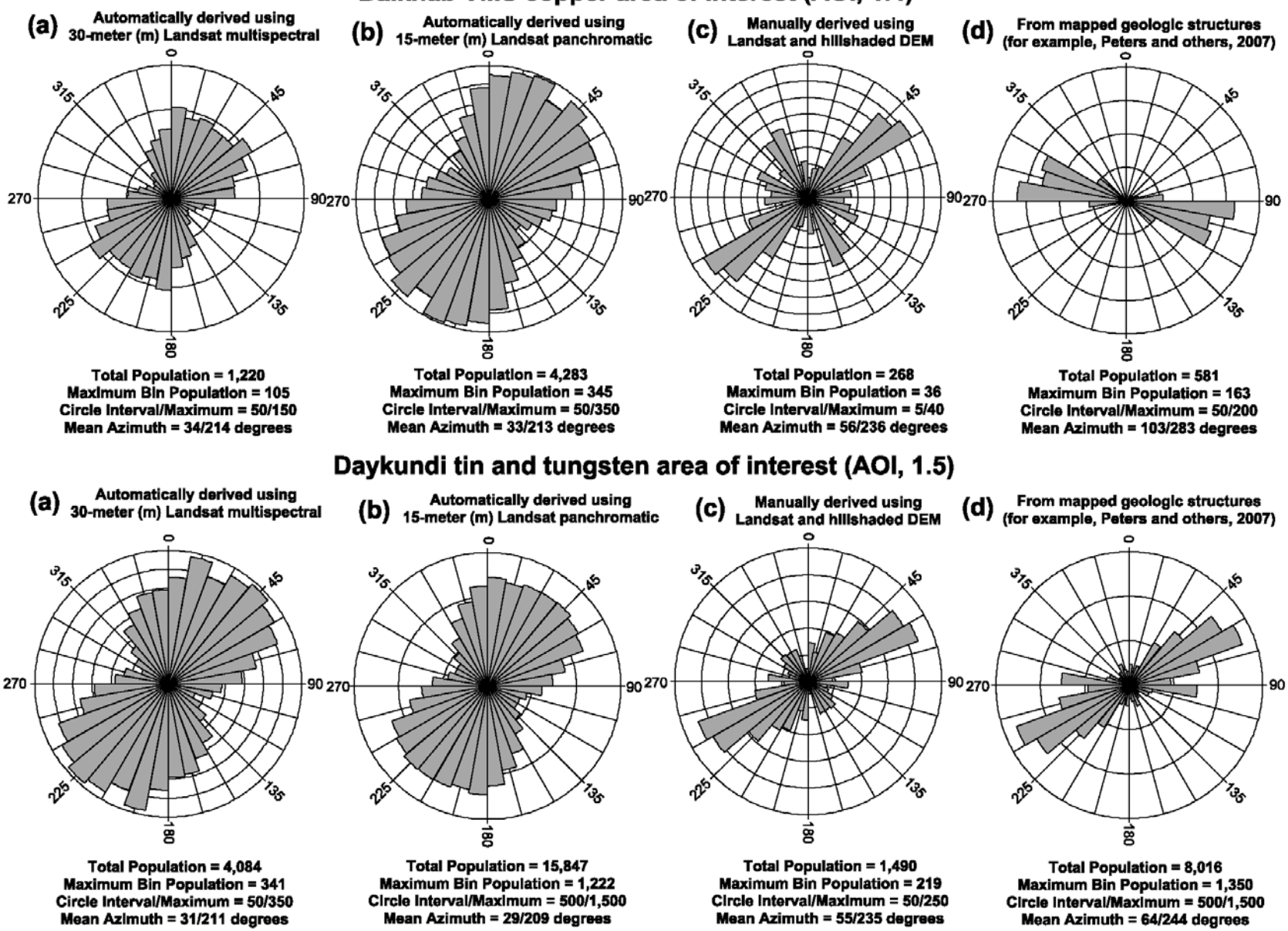
Balkhab VMS copper area of interest (AOI, 1.4)
(a) Automatically derived using 30-meter (m) Landsat multispectral
Total Population = 1,220
Maximum Bin Population = 105
Circle Interval/Maximum = 50/150
Mean Azimuth = 34/214 degrees
(b) Automatically derived using 15-meter (m) Landsat panchromatic
Total Population = 4,283
Maximum Bin Population = 345
Circle Interval/Maximum = 50/350
Mean Azimuth = 33/213 degrees
(c) Manually derived using Landsat and hillshaded DEM
Total Population = 268
Maximum Bin Population = 36
Circle Interval/Maximum = 5/40
Mean Azimuth = 56/236 degrees
(d) From mapped geologic structures (for example, Peters and others, 2007)
Total Population = 581
Maximum Bin Population = 163
Circle Interval/Maximum = 50/200
Mean Azimuth = 103/283 degrees
Daykundi tin and tungsten area of interest (AOI, 1.5)
(a) Automatically derived using 30-meter (m) Landsat multispectral
Total Population = 4,084
Maximum Bin Population = 341
Circle Interval/Maximum = 50/350
Mean Azimuth = 31/211 degrees
(b) Automatically derived using 15-meter (m) Landsat panchromatic
Total Population = 15,847
Maximum Bin Population = 1,222
Circle Interval/Maximum = 500/1,500
Mean Azimuth = 29/209 degrees
(c) Manually derived using Landsat and hillshaded DEM
Total Population = 1,490
Maximum Bin Population = 219
Circle Interval/Maximum = 50/250
Mean Azimuth = 55/235 degrees
(d) From mapped geologic structures (for example, Peters and others, 2007)
Total Population = 8,016
Maximum Bin Population = 1,350
Circle Interval/Maximum = 500/1,500
Mean Azimuth = 64/244 degrees
0
45
90
135
180
225
270
315

Dusar-Shaida copper and tin area of interest (AOI, 1.6)

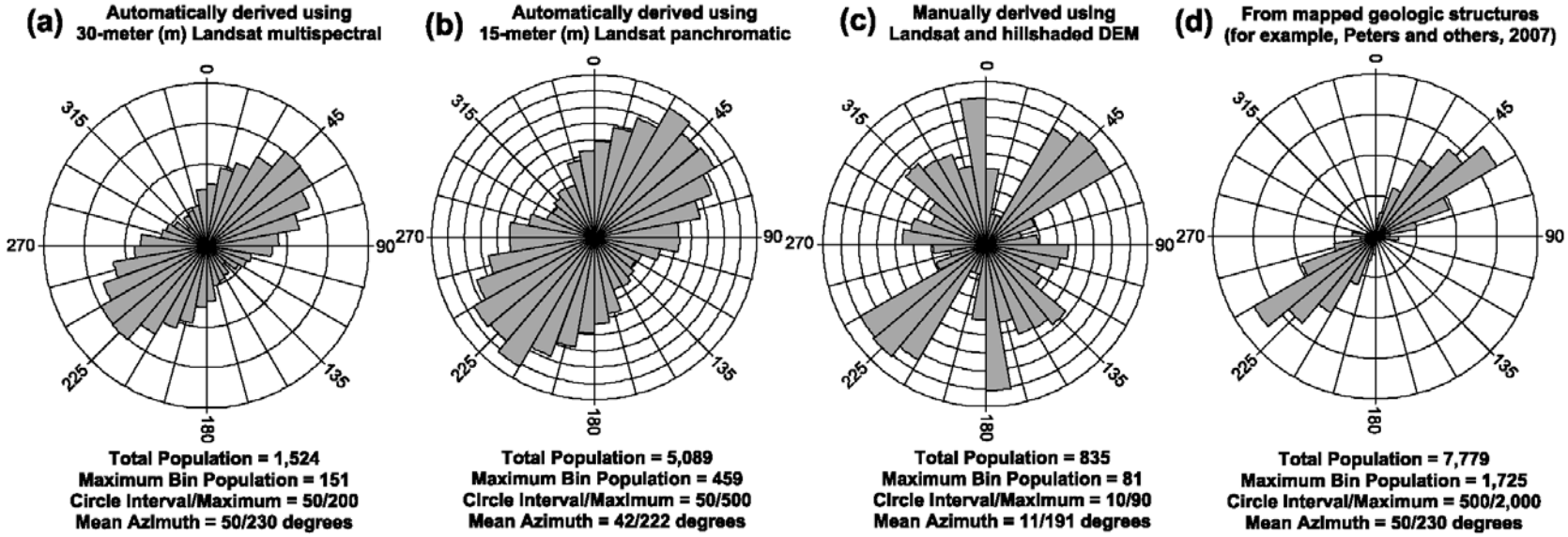

Haji-Gak iron area of interest (AOI, 1.7)

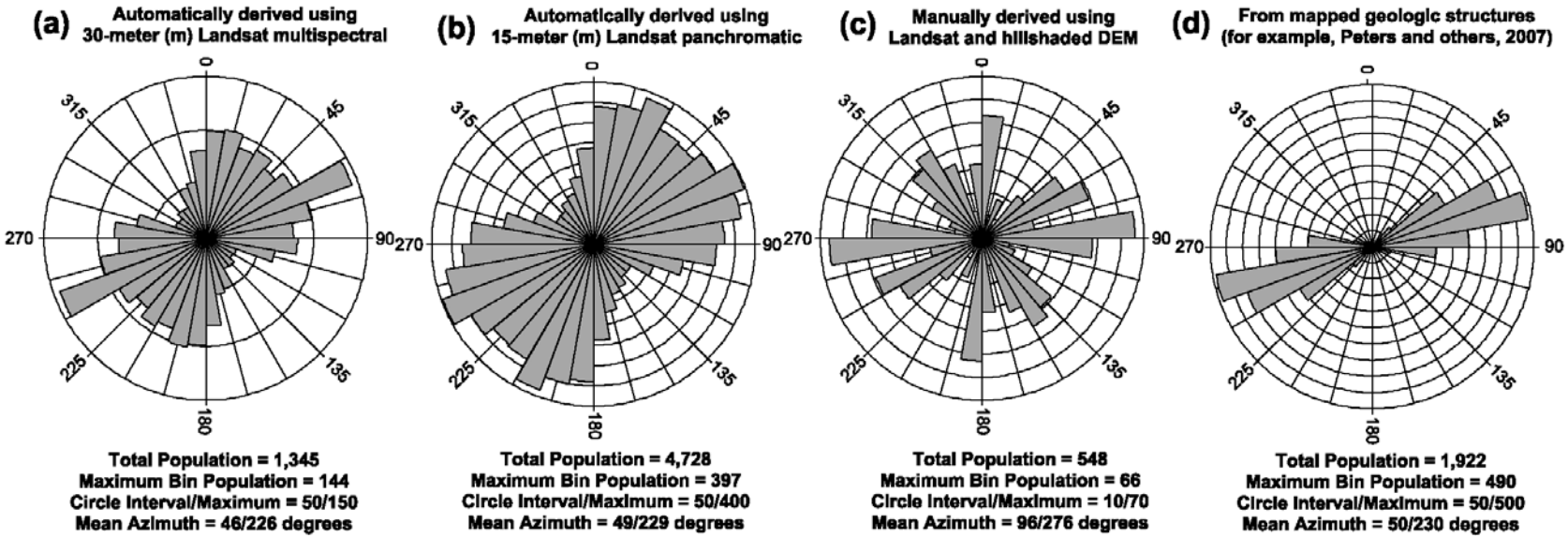

Katawas gold area of interest (AOI, 1.8)

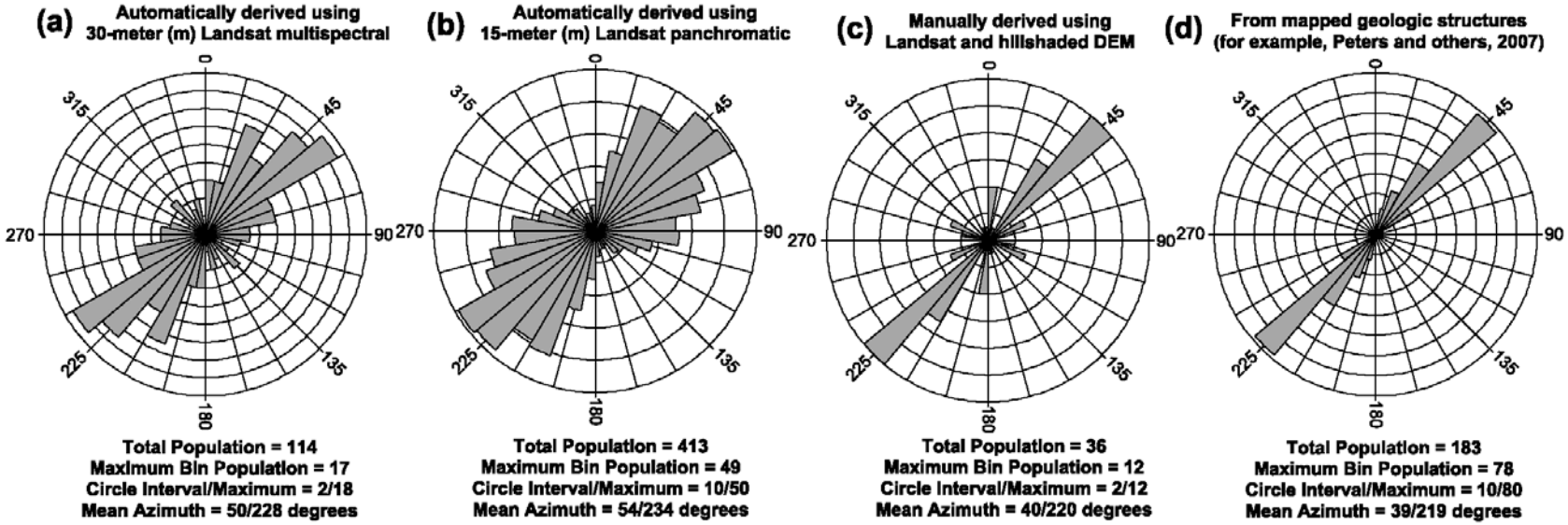

Kharnak-Kanja mercury area of interest (AOI, 1.9)

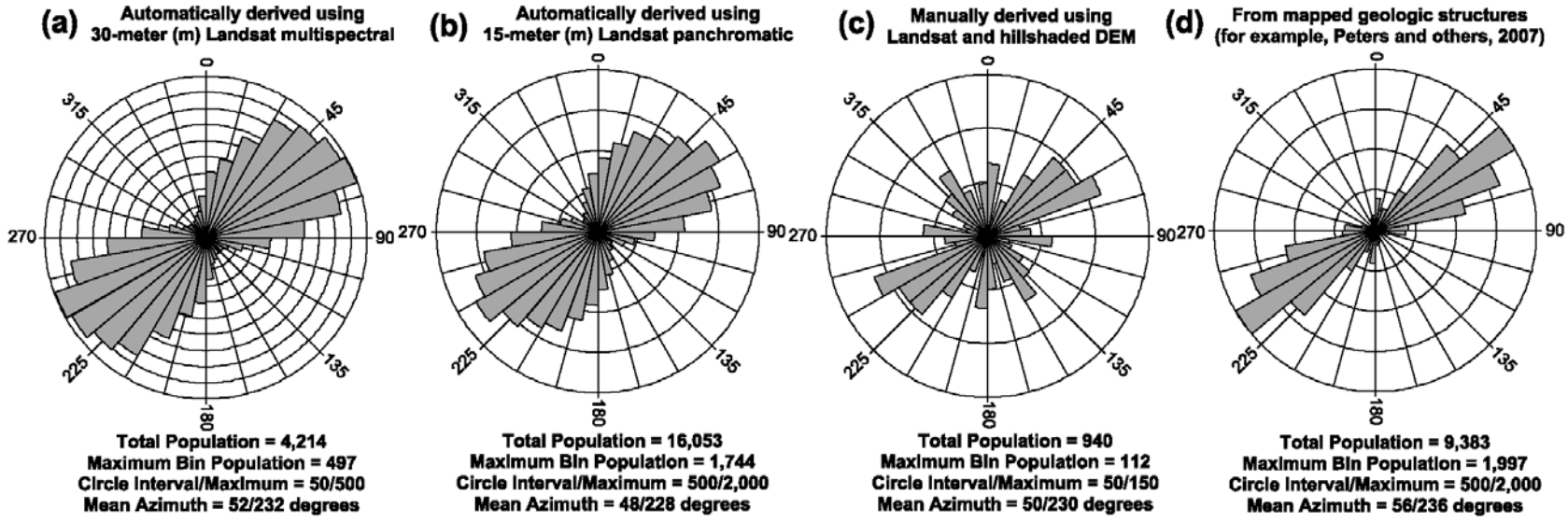

Kundalan copper and gold porphyry area of interest (AOI, 1.10)

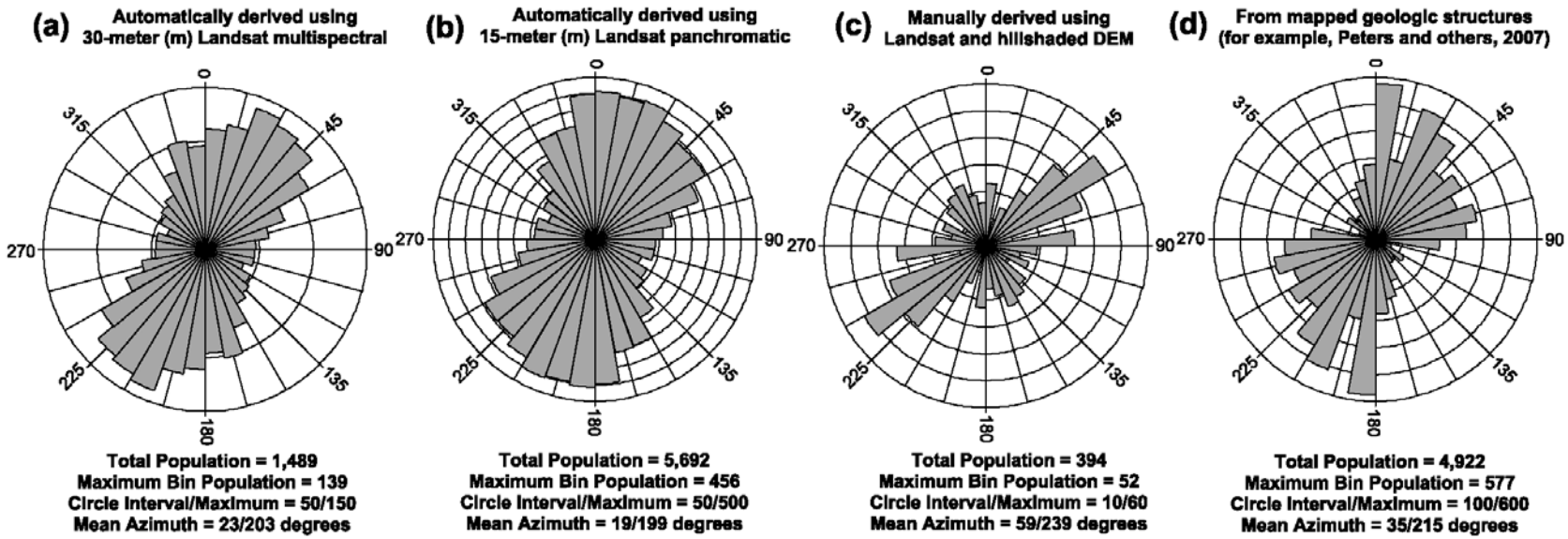

Nalbandon lead and zinc area of interest (AOI, 1.11)

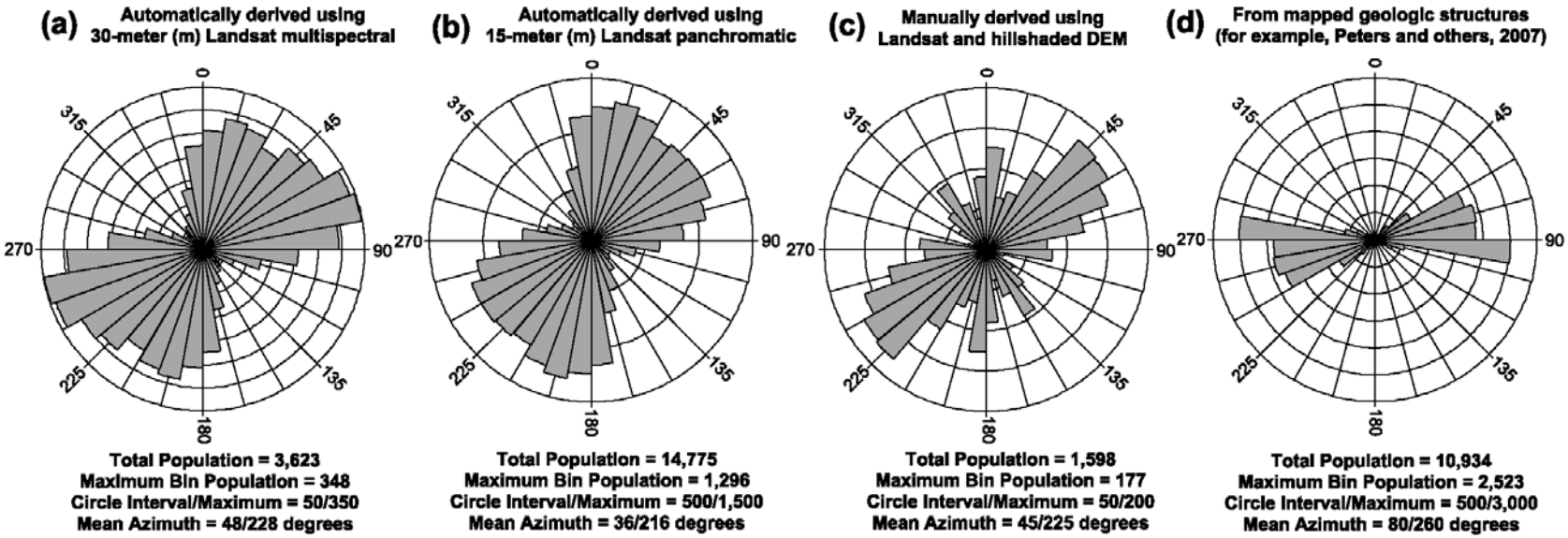

North Takhar gold-placer area of interest (AOI, 1.12)

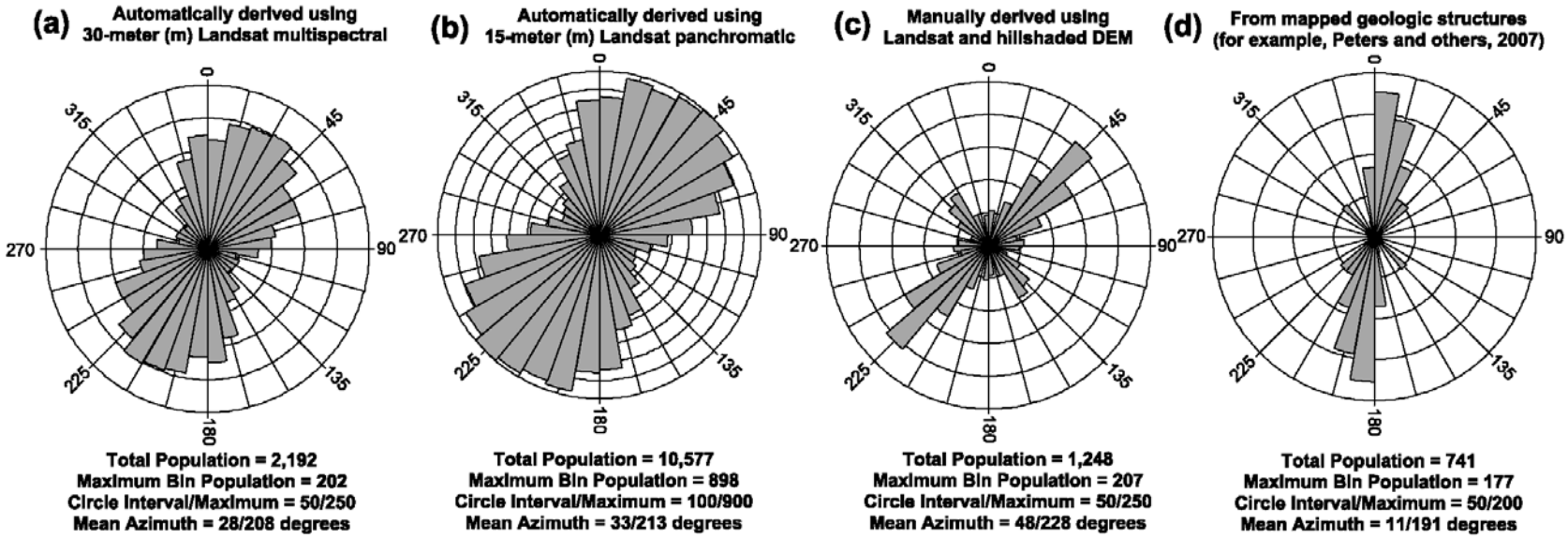

Panjsher Valley emerald, iron and silver area of interest (AOI, 1.13)

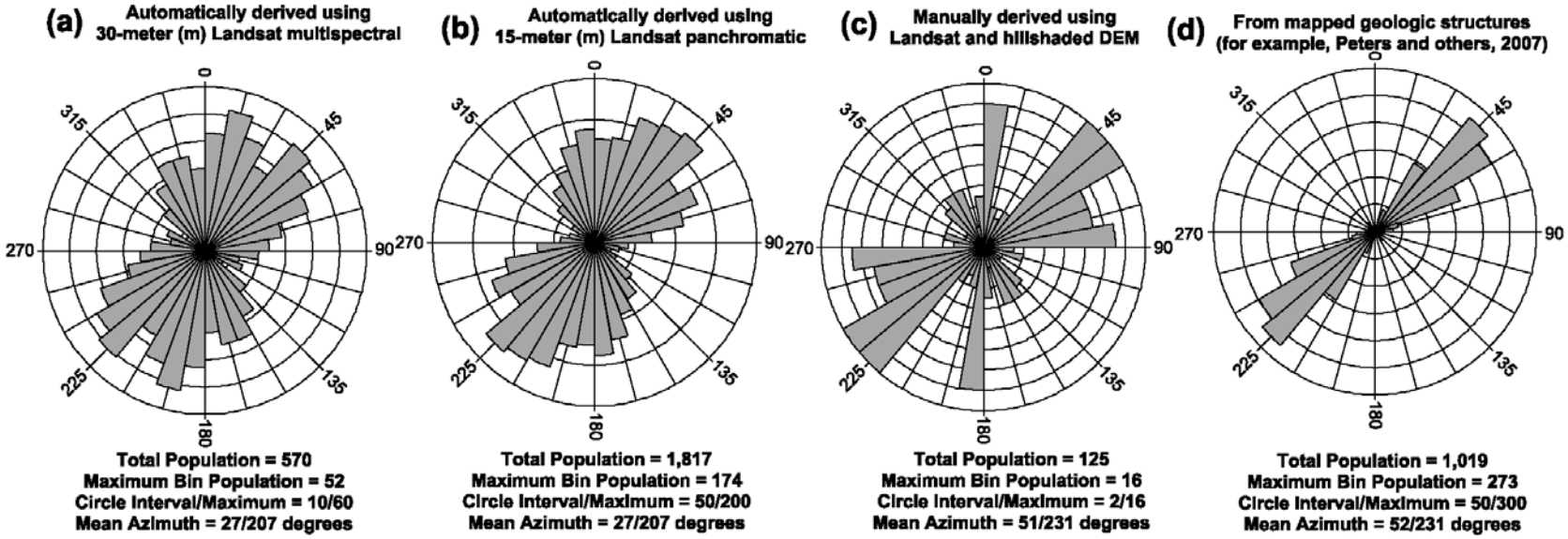

Tourmaline tin-vein area of interest (AOI, 1.14)

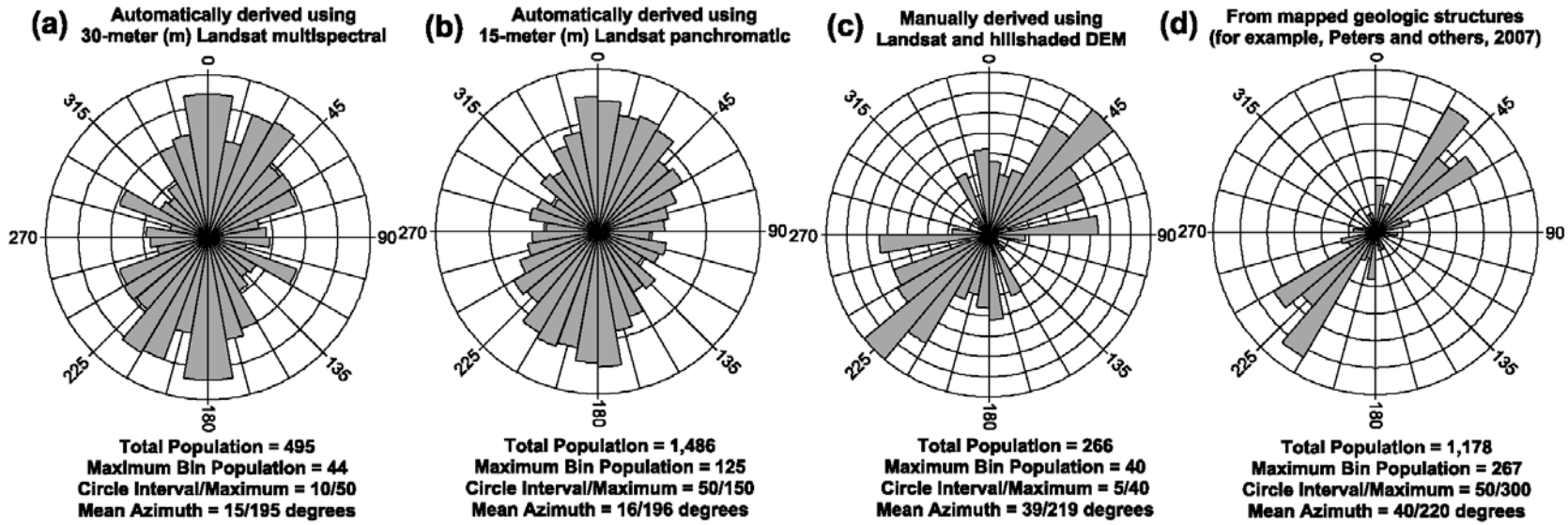

Zarkashan copper and gold area of interest (AOI, 1.15)

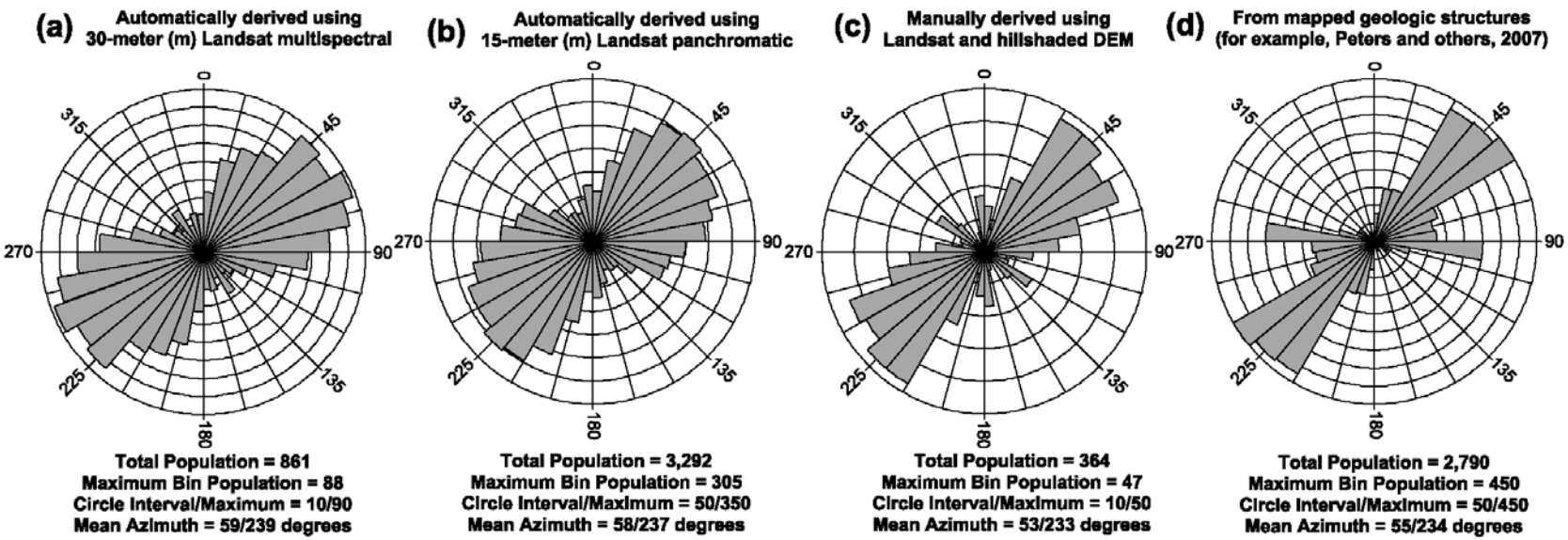

Baghlan clay and gypsum area of interest (AOI, 1.17)

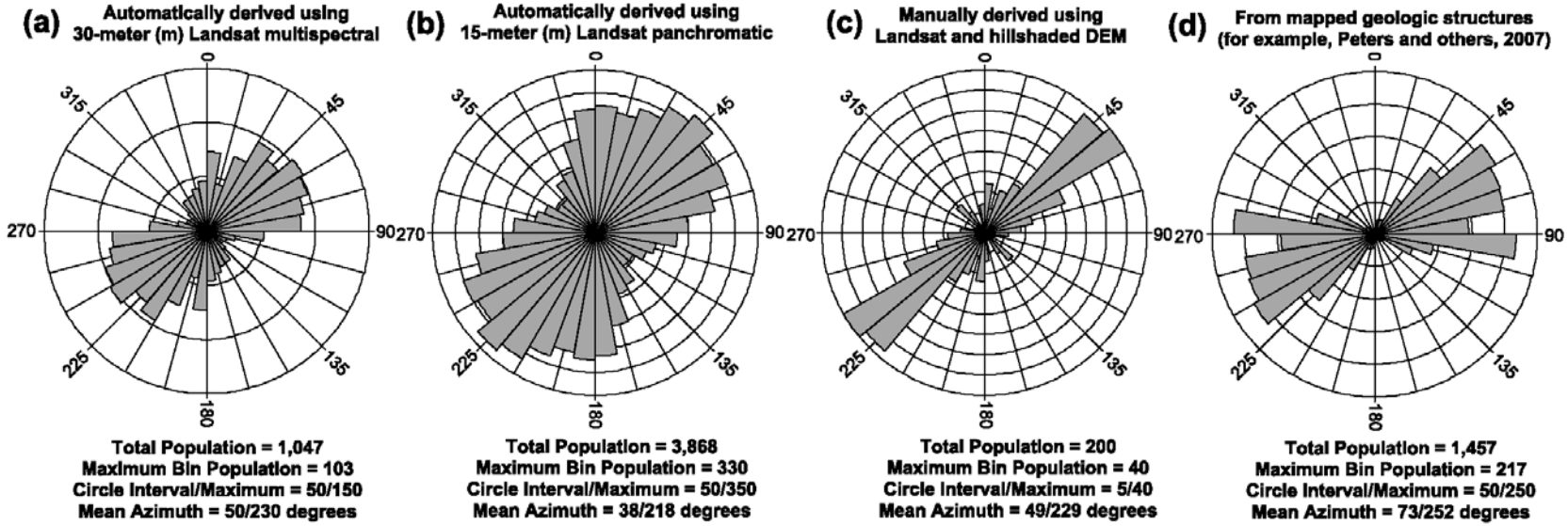

Bakhud flourite area of interest (AOI, 1.18)

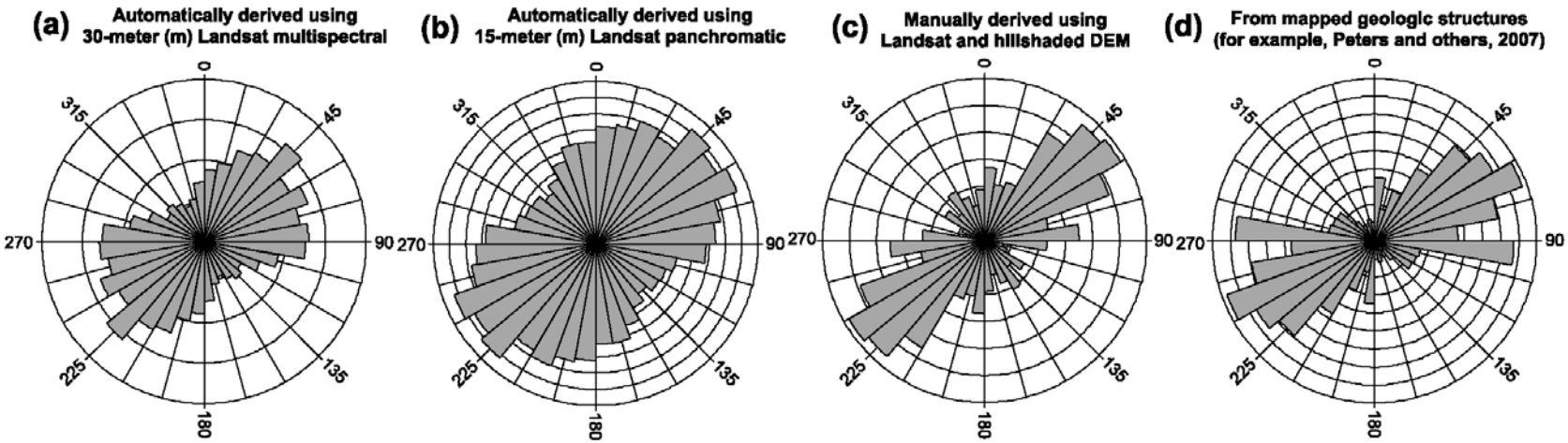

Dudkash industrial minerals area of interest (AOI, 1.19)

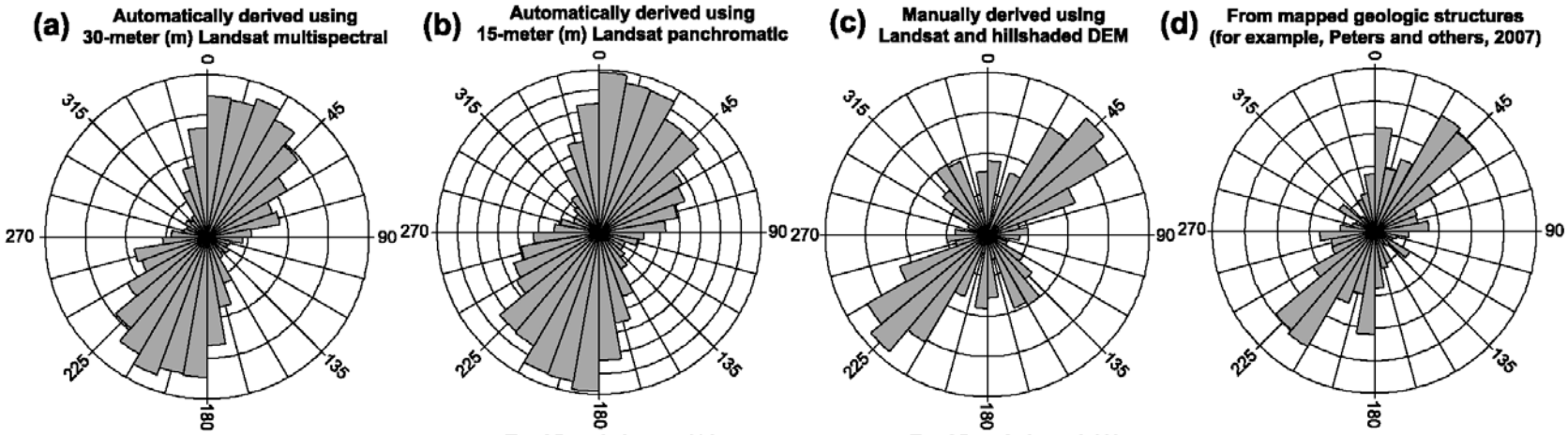

Ghunday-Achin magnesite and talc area of interest (AOI, 1.20)

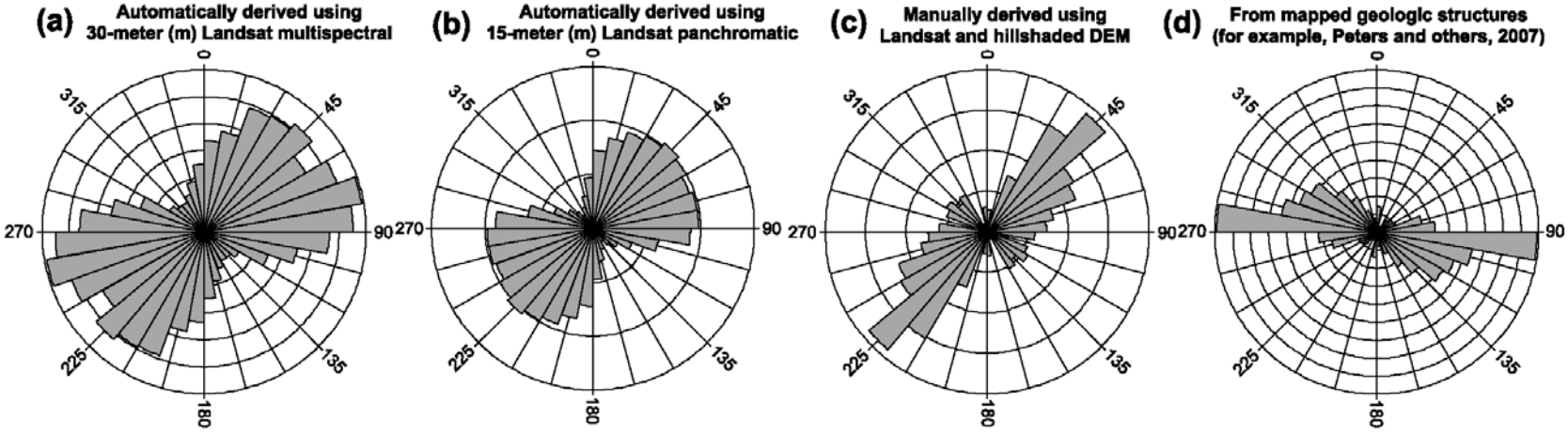

Khanneshin carbonatite area of interest (AOI, 1.21)

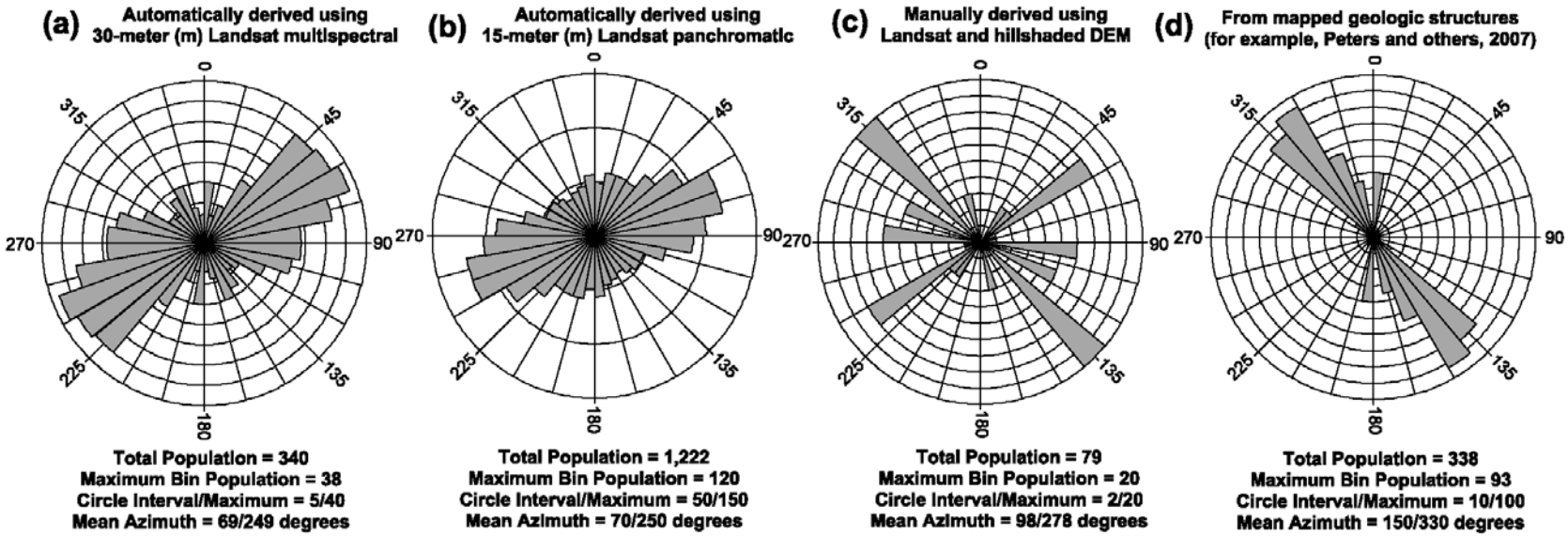

Kunduz celestite area of interest (AOI, 1.22)

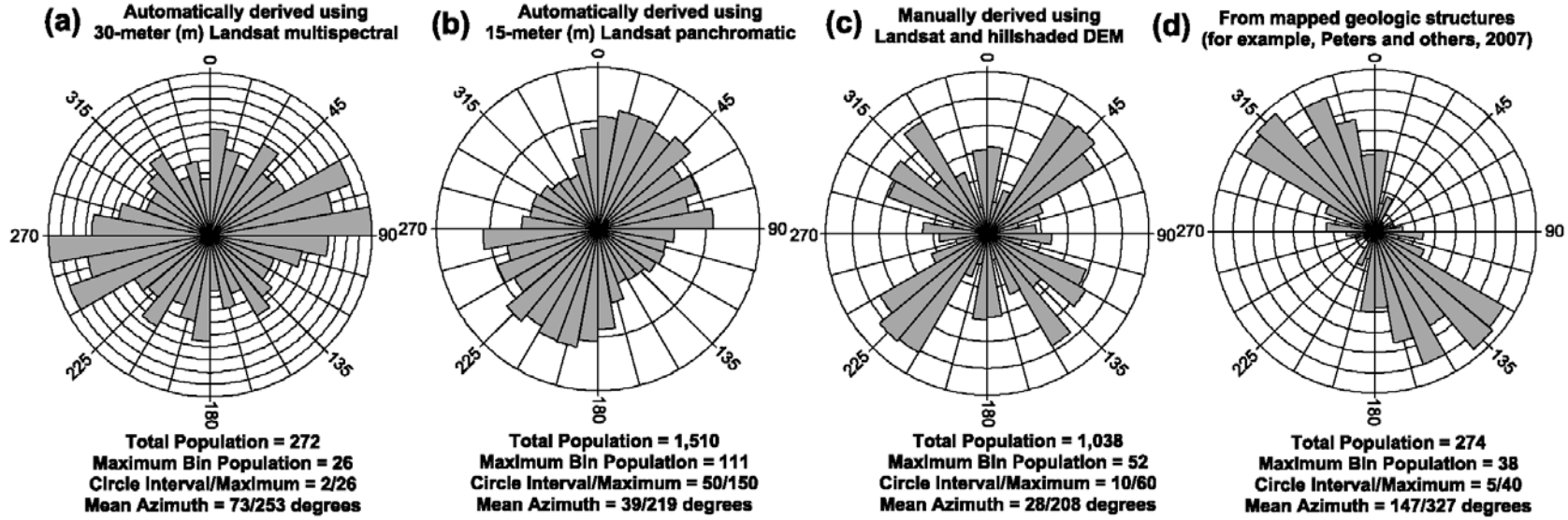

North Herat barium and limestone area of interest (AOI, 1.23)

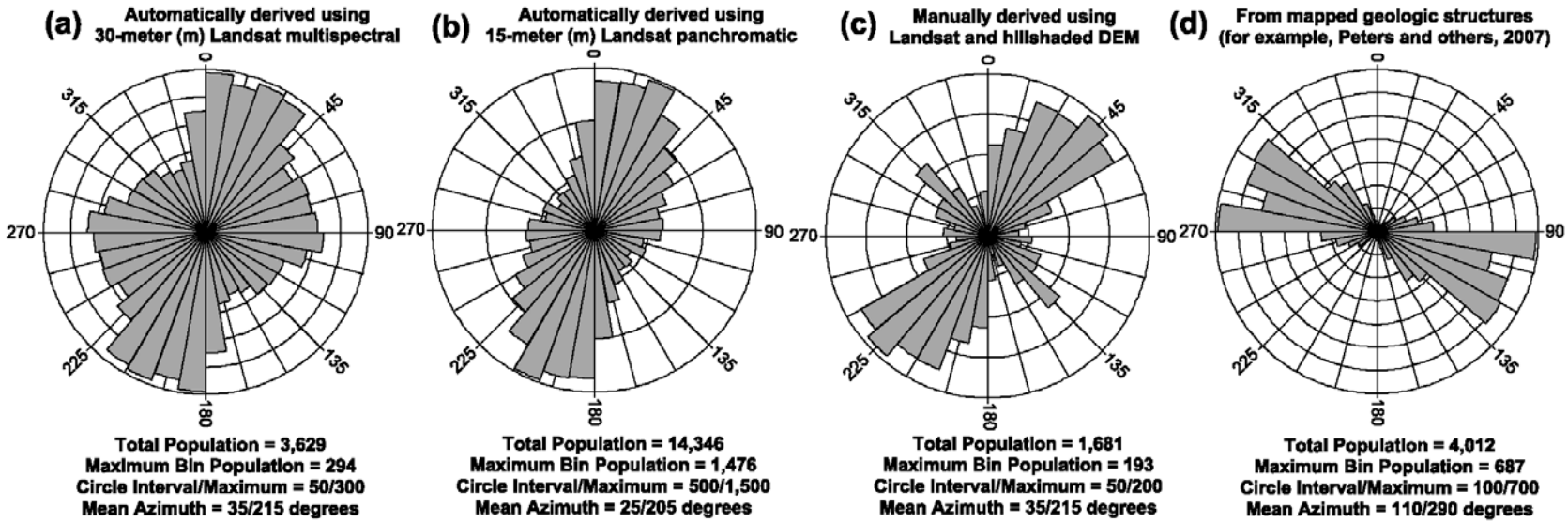

Nuristan pegmatite area of interest (AOI, 1.24)

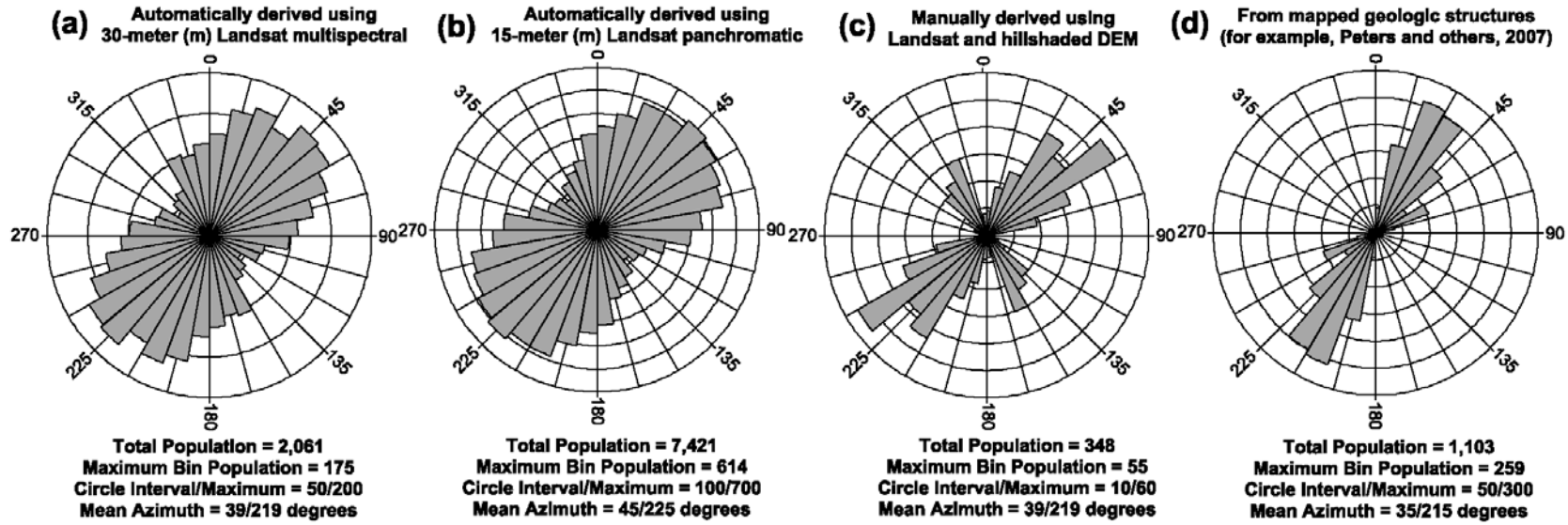

South Helman travertine area of interest (AOI, 1.25)

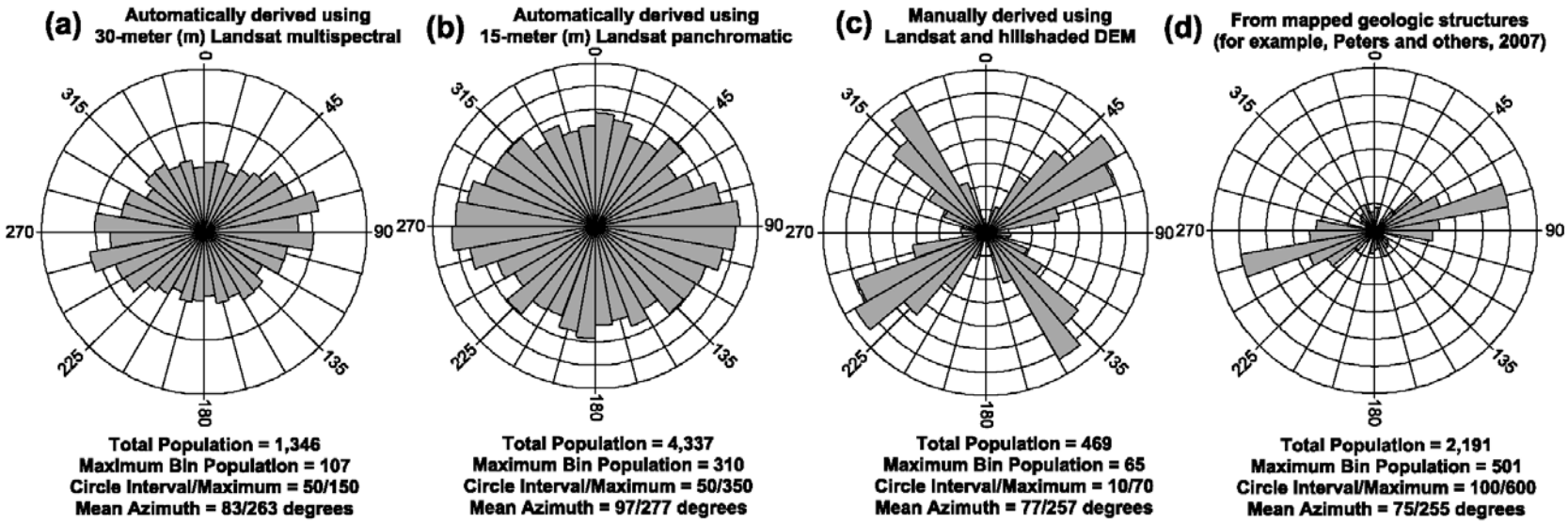

Takhar evaporite area of interest (AOI, 1.26)